journal of the mechanical behavior of biomedical materials 128 (2022) 105118

Contents lists available at ScienceDirect

Journal of the Mechanical Behavior of Biomedical Materials

journal homepage: www.elsevier.com/locate/jmbbm

Research paper

A micro-mechanical model for the fibrous tissues of vocal folds

Alberto Terzolo [a], Lucie Bailly [a,*], Laurent Orgéas [a], Thibaud Cochereau [a,b], Nathalie Henrich Bernardoni [b]

[a] Univ. Grenoble Alpes, CNRS, Grenoble INP, 3SR, 38000 Grenoble, France
[b] Univ. Grenoble Alpes, CNRS, Grenoble INP, GIPSA-lab, 38000 Grenoble, France

ARTICLE INFO

Keywords:
Vocal folds
3D fibrous architecture
Micro-mechanical model
Anisotropy
Multiaxial loading
Vibratory properties

ABSTRACT

Composed of collagen, elastin and muscular fibrous networks, vocal folds are soft laryngeal multi-layered tissues owning remarkable vibro-mechanical performances. However, the impact of their histological features on their overall mechanical properties still remains elusive. Thereby, this study presents a micro-mechanical hyperelastic model able to describe the 3D fibrous architecture and the surrounding matrices of the vocal-fold sublayers, and to predict their mechanical behavior. For each layer, the model parameters were identified using available histo-mechanical data, including their quasi-static response for key physiological loading paths, *i.e.,* longitudinal tension, transverse compression and longitudinal shear. Regardless of the loading path, it is shown how macroscale nonlinear, anisotropic tissue responses are inherited from the fiber scale. Scenarios of micro-mechanisms are predicted, highlighting the major role of 3D fiber orientation in tension, steric hindrance in compression, and matrix contribution in shear. Finally, combining these predictions to vibrating hyperelastic Timoshenko beam's theory, the impact of the fibrous architecture of the upper layers on vocal-fold vibratory properties is emphasized.

1. Introduction

Human vocal folds possess a complex lamellar structure with two principal layers: the *lamina propria*, *i.e.,* a loose connective tissue, and the *vocalis* or inferior thyroarytenoid muscle. Each layer is a soft material with architectured networks of collagen, elastin and/or skeletal muscle fibers (Fig. 1; Hirano, 1974; Bühler et al., 2011; Bailly et al., 2018). Clinical observations clearly support the major role played by such fibrous microstructure in the vocal-fold vibrations: in cases of benign or cancerous lesions, alterations of the fiber-scale arrangement of the *lamina propria* systematically induce a vibratory dysfunction (Finck, 2008; Finck et al., 2010; Hantzakos et al., 2009); with aging, a loss of elastin fibers, fibrosis or muscle atrophy together with vocal and perceptual changes such as hoarseness, low pitch and breathiness has also been observed (Sato and Tauchi, 1982; Sato et al., 2002; Roberts et al., 2011). However, to date, the acquired knowledge is still not sufficient to understand the relationship between the microstructural specifications of vocal folds and their macroscale performances.

This is mainly ascribed to their challenging experimental multiscale characterization. Despite the considerable progress made in 3D micro-imaging (Herrera et al., 2009; Kobler et al., 2010; Chen et al., 2013; Miri et al., 2012; Klepacek et al., 2016; Garcia et al., 2016; Bailly et al., 2018; Kazarine et al., 2019), vocal folds, along with their fibrous architectures, are hardly observable *in vivo* (Maturo et al., 2012; Coughlan et al., 2016). Although a large biomechanical database has been collected on excised vocal folds over the last twenty years (Chan et al., 2001; Rohlfs et al., 2013; Kelleher et al., 2013a; Miri et al., 2014; Chan, 2018; Cochereau et al., 2020), the 3D microscale rearrangement of the loaded tissues is still to be explored. Conversely, the development of macroscopic (tissue scale) or micro-mechanical (fiber scale) models of phonation is a promising alternative to gain an in-depth understanding of the vocal-fold biomechanics:

- In macroscopic approaches, phenomenological exponential and power-law functions are commonly proposed to describe the stress–strain responses typically observed when deforming soft biological tissues (Basciano and Kleinstreuer, 2009; Hollingsworth and Wagner, 2011; Holzapfel et al., 2000; Limbert and Middleton, 2006; Lin and Yin, 1998; May-Newman et al., 2009). Doing so, however, the model parameters can hardly be related to the material intrinsic structure and mechanics, and need to be adjusted according to the applied loading path. This first approach is robust and adequate in absence of tissue histo-mechanical data.
- Microstructure-based formulations are instead inspired from histological evidence, and conceived to correlate the model input

* Correspondence to: Laboratoire 3SR, Domaine Universitaire BP53, 38041 GRENOBLE Cedex 9, France.
E-mail address: lucie.bailly@3sr-grenoble.fr (L. Bailly).

https://doi.org/10.1016/j.jmbbm.2022.105118
Received 29 October 2021; Received in revised form 14 January 2022; Accepted 3 February 2022
Available online 16 February 2022

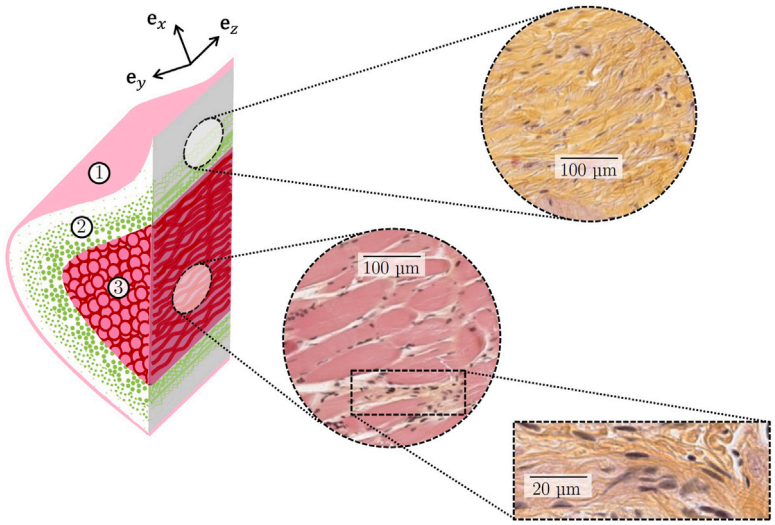

Fig. 1. Human vocal-fold histology. *(left)* Idealized scheme of one fold, with focus on the fold sublayers and fibrous microstructure: ① *Epithelium*, ② *Lamina propria*, ③ *Vocalis* muscle. *(right)* Corresponding 2D histological photomicrographs prepared with HES staining: collagen fibers (yellow–orange); cytoplasms, striated muscular and elastin fibers (pink); *nuclei* (black–purple) .
Source: Adapted from Cochereau et al. (2020).

parameters to the physical and structural properties of the tissue (*e.g.,* cells, fibers and surrounding matrix). To name a few, the shape, concentration, orientation and tortuosity of fibers are the relevant structural parameters that are commonly considered. Therefrom, to determine the macroscale mechanical behavior of the tissue, homogenization techniques (Maceri et al., 2010a,b, 2013; Marino and Vairo, 2013, 2014b,a; Nierenberger et al., 2013; Bailly et al., 2012), energetic approaches (Miri et al., 2013; Natali et al., 2009; Ogden and Saccomandi, 2007; Pinsky et al., 2005; Peng et al., 2006), statistical descriptions (Chen et al., 2013; Gasser et al., 2006; Lanir, 1983; Kastelic et al., 1980) or variational considerations (Comninou and Yannas, 1976; Freed and Doehring, 2005; Lanir, 1978; Marino and Vairo, 2012; Marino and Wriggers, 2017) are used. Regardless, the identification and validation of these formulations with multiscale experimental data remains a challenging task.

By contrast with many other soft tissues (*e.g.,* arteries, heart, skin), the majority of the theoretical approaches adopted to model the vocal-fold mechanical properties still rely on macroscopic formulations. Since 2010, a few authors have proposed micro-mechanical models for the vocal-fold tissues, opening a new insight into voice biomechanics (Kelleher et al., 2013a; Miri et al., 2013). These models allow to predict the tensile behavior of the *lamina propria*, but their relevance was not assessed for other important biomechanical loadings such as transverse compression and longitudinal shear (Gunter, 2003; Tao and Jiang, 2007; Vampola et al., 2016). Furthermore, theoretical formulations still need: (i) to be fed up with 3D microstructural descriptors of human vocal-fold sublayers and to account for the fiber-to-fiber mechanical interactions likely to occur within such dense media (Ekman et al., 2014), (ii) to be extended to the specific micro-arrangement of the *vocalis* muscle.

Within this context, the present work proposes a micro-mechanical model able to reproduce the nonlinear anisotropic mechanical properties of vocal-fold layers (*i.e., lamina propria*, *vocalis*) subjected to multiaxial finite strains, from the knowledge of their 3D fibrous architecture. It combines the use of *ex vivo* database acquired on human vocal-fold microstructures over the past ten years, with a recent study on their finite strain macroscale mechanics in longitudinal tension, as well as transverse compression and longitudinal shear (Cochereau et al., 2020). The paper is structured as follows. Section 2 introduces an improvement of the theoretical formulation firstly proposed and validated in the context of vascular biomechanics (Bailly et al., 2012, 2014). The model identification procedure is described in Section 3. Section 4 presents the vocal-fold multiscale predictions and a micro-parametrical study aimed to investigate the effect of the tissue's 3D fibrous orientation changes on its vibro-mechanical response.

2. Micro-mechanical model

2.1. Experimental observations and assumptions

In line with histological evidence (Fig. 1; Bailly et al. (2018), Madruga de Melo et al. (2003), Hammond et al. (1997), Kelleher et al. (2013b), Miri et al. (2013)), both the *lamina propria* and the *vocalis* can be conceived as 3D incompressible composite structures made of a gel-like matrix reinforced by a network of fibers. Furthermore, each fiber can in turn be seen as a bundle of quasi-aligned (myo)fibrils with wavy shapes and preferred orientations at rest:

- The *lamina propria* is made of cells and an extracellular matrix (ECM) comprising amorphous ground substances (*e.g.,* hyaluronic acid), entangled fibrous networks of collagen (mainly Type I and III) and elastin (Miri et al., 2012). Collagen plays a key role in the mechanics of soft tissues and is, by weight, the most abundant fibrous protein in the human *lamina propria*, representing at least 50% of the total proteins (less than 10% for elastin (Hahn et al., 2006a,b; Tateya et al., 2006)). The *lamina propria* is finally known to be arranged in three sublayers with distinct fibers' type, density and arrangement, albeit very challenging to model due to the lack of available quantitative topological descriptors. In the following, the multilayered tissue of the *lamina propria* is therefore simplified to a one-layered structure. The fibrous network of its ECM is assumed to include a single population of collagen fibers, *i.e.,* fiber bundles of collagen fibrils, embedded into a surrounding matrix gathering the other neighboring tissue components (cells, elastin, ground substances).
- The *vocalis* is primarily made of muscle fibers (also called "muscle cells" or "rhabdomyocytes"), grouped into fiber bundles (or *fasciculi*) and wrapped together by connective tissue sheaths (Fig. 1; Bailly et al. (2018)). This muscle ECM is dominated by collagen in terms of mass, and is organized into three interconnected levels: the *epimysium*, surrounding the whole muscles, the

perimysium, surrounding fascicles, and the *endomysium*, surrounding individual muscle fibers (Borg and Caulfield, 1980; Ward et al., 2020). Collagen has been recently shown to be a major load-bearing component in the finite strain passive response of skeletal muscles (Ward et al., 2020). Therefore, in the following, each individual muscle fiber is conceived as a myofibrils bundle surrounded by a sheath of collagen fibers (*i.e.,* bundles of collagen fibrils). The other constituents of the skeletal muscle ECM (elastin, proteoglycans, glycoproteins) will constitute the matrix of the micro-mechanical model (Csapo et al., 2020).

2.2. Idealization of the vocal-fold layers' fibrous architectures

Regardless of the considered vocal-fold layer (*i.e., lamina propria* or *vocalis*), its microstructure is idealized by the periodic repetition of a Representative Elementary Volume (REV) inspired from that already proposed for rubber-like materials (Arruda and Boyce, 1993; Boyce and Arruda, 2000; Beatty, 2003) or self-entangled superelastic wires (Rodney et al., 2016), as sketched in Fig. 2a. In the undeformed configuration $\mathcal{C}_0$ (resp. deformed configuration $\mathcal{C}$), the REVs can be seen as prisms with a truss of $N = 4$ bars, of identical initial length ℓ_0 (resp. actual lengths ℓ_i), embedded in a matrix and connected to a central node C_0 (resp. c_0) and to the nodes C_i (resp. c_i), $i \in [1, \dots, N]$ of corresponding neighboring REVs at their extremities. The initial (resp. actual) orientation of each bar i is denoted by the direction of its unit vector $\mathbf{E}_i = \mathbf{C}_0\mathbf{C}_i/\|\mathbf{C}_0\mathbf{C}_i\| = \sin\theta_{0i}\cos\varphi_{0i}\,\mathbf{e}_x + \sin\theta_{0i}\sin\varphi_{0i}\,\mathbf{e}_y + \cos\theta_{0i}\,\mathbf{e}_z$ (resp. $\mathbf{e}_i = \mathbf{c}_0\mathbf{c}_i/\|\mathbf{c}_0\mathbf{c}_i\| = \sin\theta_i\cos\varphi_i\,\mathbf{e}_x + \sin\theta_i\sin\varphi_i\,\mathbf{e}_y + \cos\theta_i\,\mathbf{e}_z$) where $\mathbf{e}_x$, $\mathbf{e}_y$ and $\mathbf{e}_z$ lie along the medio-lateral, infero-superior and antero-posterior anatomical directions (Fig. 1). In the following, considering the typical orthogonal symmetry planes previously found in the vocal-fold fibrous architectures at rest (Kelleher et al., 2013a; Bailly et al., 2018), we further assume that the initial angles of the fibrous networks do not depend on the bar i: $\forall i$, $\theta_{0i} = \theta_0$ and $\varphi_{0i} = \pm\varphi_0 \mp k\pi$, $k \in [0, 1]$.

Therefrom, as illustrated in Fig. 2b, each bar i represents the chord of a wavy (collagen or muscle) fiber bundle i. Additionally, each fiber bundle i is considered as an assembly of n identical and parallel fibrils of equal waviness and length. Furthermore, each fibril j is defined by its initial diameter d_0, length ℓ_0^f (resp. actual ℓ_j^f), and tortuosity $\xi_0 = \ell_0^f/\ell_0$ (resp. $\xi_j = \ell_j^f/\ell_i$). A monomodal sinusoidal function is used to describe each fibril's initial waveform of amplitude R_0 and spatial periodicity H_0 (Comninou and Yannas, 1976; Lanir, 1979; Miri et al., 2013), *i.e.,* with $v(u) = R_0 \sin\frac{2\pi}{H_0}u$ in the reference frame $(\mathbf{u}_j, \mathbf{v}_j)$ of fibril j sketched in Fig. 2, where u and v are the abscissa and ordinate in $(\mathbf{u}_j, \mathbf{v}_j)$, respectively. We assumed the bars to contain 10 typical sinusoidal periods between nodes. This arbitrary choice is not a restriction. Therewith:

- In the *lamina propria* (Fig. 2b-i), the volume fraction of fibrils in the REV is $\Phi = V_f/V_{REV}$, where $V_{REV} = 4\ell_0^3\sin^2\theta_0\cos\theta_0\cos\varphi_0\sin\varphi_0$ is the volume of the REV and where $V_f = \pi N n d_o^2 \ell_0^f/4$ with $\ell_0^f = \int_0^{\ell_0}\sqrt{1 + (\frac{2\pi R_0}{H_0}\cos(\frac{2\pi}{H_0}u))^2}\,du$.
- In the *vocalis* (Fig. 2b-ii), even if collagen and muscle fibers are referred to the same bar (with the same mean orientation (θ_i, ϕ_i)), each family of fibrils is characterized by distinct geometrical parameters, labeled with subscript c (resp. m) for collagen (resp. muscular) fibrils. Thus the volume fraction of fibrils is decomposed as follows: $\Phi = \Phi_c + \Phi_m$, where Φ_c and Φ_m are the volume fractions of collagen and myofibrils, respectively, with waveform parameters H_{0k}, R_{0k} and diameters d_{0k}, $k \in \{c, m\}$.

2.3. Micro-mechanical behavior of the constitutive materials

Matrix – Independently of the vocal-fold sublayer, the gel-like matrix is conceived as a soft isotropic, hyperelastic and incompressible material, as a first reasonable approximation. The corresponding mechanical behavior is described by a simple neo-Hookean model (Treloar, 1943), characterized by a volumetric strain–energy function $W = 0.5\,\mu(1 - \Phi)(I_1 - 3)$, where μ is the shear modulus of the matrix, and $I_1 = \mathrm{tr}(\mathbf{B})$ where $\mathbf{B} = \mathbf{F}\cdot\mathbf{F}^T$ ($\mathbf{F}$ being the macroscopic transformation gradient).

Fibrils

Tension – As sketched in Fig. 3(a), when stretched with a strain $\varepsilon_j = \ln\frac{\ell_j}{\ell_0}$, the mechanics of wavy fibrils is firstly dominated by their progressive unfolding (regimes (i) and (ii)), up to a critical strain $\varepsilon_c = \ln\xi_0$ once fully unfolded ($\ell_j = \ell_0^f$). Past this threshold, fibrils behave as straight elastic rods showing a quasi-linear tensile response (regime (iii)) with a Young modulus E_f (Colomo et al., 1997; Gautieri et al., 2012). These two regimes, as well as the transition in between, are well described by the following constitutive relation (Orgéas et al., 1998):

$$\mathbf{t}_j = \frac{\pi d_0^2}{4}\left[E_{eq0}\varepsilon_j + \frac{E_f - E_{eq0}}{2} \times \left(\varepsilon_j + \sqrt{(\varepsilon_j - \ln\xi_0)^2 + \alpha^2} - \sqrt{\ln^2\xi_0 + \alpha^2}\right)\right]\mathbf{e}_i \tag{1}$$

where $\mathbf{t}_j$ is the tension along the fibril j. In this last equation, α is a parameter that ensures a smooth transition between the two aforementioned regimes. Additionally, E_{eq0} is the initial tangent modulus measured on $(t_j\ ,\ \varepsilon_j)$ curves. Its expression can be analytically obtained (Potier-Ferry and Siad, 1992):

$$E_{eq0} = E_f\,\langle\cos\beta_0\rangle\,/[\ \langle\cos^2\beta_0\rangle + 16\,\langle v^2\rangle\,/d_0^2\ ] \tag{2}$$

where $\langle\cdot\rangle = \frac{1}{\ell_0}\int_0^{\ell_0}\cdot\,du$, $\beta_0 = \arctan\left(2\pi\frac{R_0}{H_0}\cos\frac{2\pi}{H_0}u\right)$ and $\langle v^2\rangle = R_0^2/2$.

In the particular case of the *vocalis* (see Fig. 2b-ii), note that the tension force $\mathbf{t}_{jk}$ within each type of fibrillar networks (collagen or muscular) is characterized by distinct fibril's Young modulus E_{fk} and toe-region parameter α_k.

Compression – The stiffening regime (ii)–(iii) occurring in tension is not prone to occur during the compression of fibrils. Instead, fibrils should rather increase their crimping. To account for this tension–compression asymmetry, from Eq. (1), we simply assumed that fibrils compression follows the same tendency detailed in tension during regime (i) solely:

$$\mathbf{t}_j = \frac{\pi d_0^2}{4}E_{eq0}\,\varepsilon_j\,\mathbf{e}_j \tag{3}$$

Fibers – Between nodes, fiber bundles can be seen as wavy beams of parallel fibrils (Fig. 2(b)), whose transverse shear interactions are significantly weaker than their longitudinal tensile behavior. Therefrom, the tension–compression force $\mathbf{T}_i$ in the fiber is simply expressed (with $N = 4$) as:

$$\mathbf{T}_i = \sum_{j=1}^{n}\mathbf{t}_j = n\,\mathbf{t}_i = \frac{\Phi V_{REV}}{\pi d_0^2\ell_0^f}\mathbf{t}_i \tag{4}$$

In the case of two fibrils families (*vocalis*), this generic equation comes:

$$\mathbf{T}_i = \frac{V_{REV}}{\pi}\left(\frac{\Phi_c}{d_{0c}^2\ell_0\xi_{0c}}\mathbf{t}_{\mathbf{ic}} + \frac{\Phi_m}{d_{0m}^2\ell_0\xi_{0m}}\mathbf{t}_{\mathbf{im}}\right) \tag{5}$$

Fiber-to-fiber interactions: steric hindrance – When fibrous networks are subjected to mechanical loading, the resulting deformation does not solely arise from the (un)folding of fiber bundles, which may also rotate and get closer. These motions are physically constrained by steric hindrance, so that they generate fiber-to-fiber interactions (Ekman et al., 2014). These constraints are not taken into account in the standard eight chains model (Arruda and Boyce, 1993) whereas they should alter the REV deformation micro-mechanisms and thus its macroscale properties. Therefore, in this first approach, we added repulsive forces between neighbored unconnected nodes of the truss

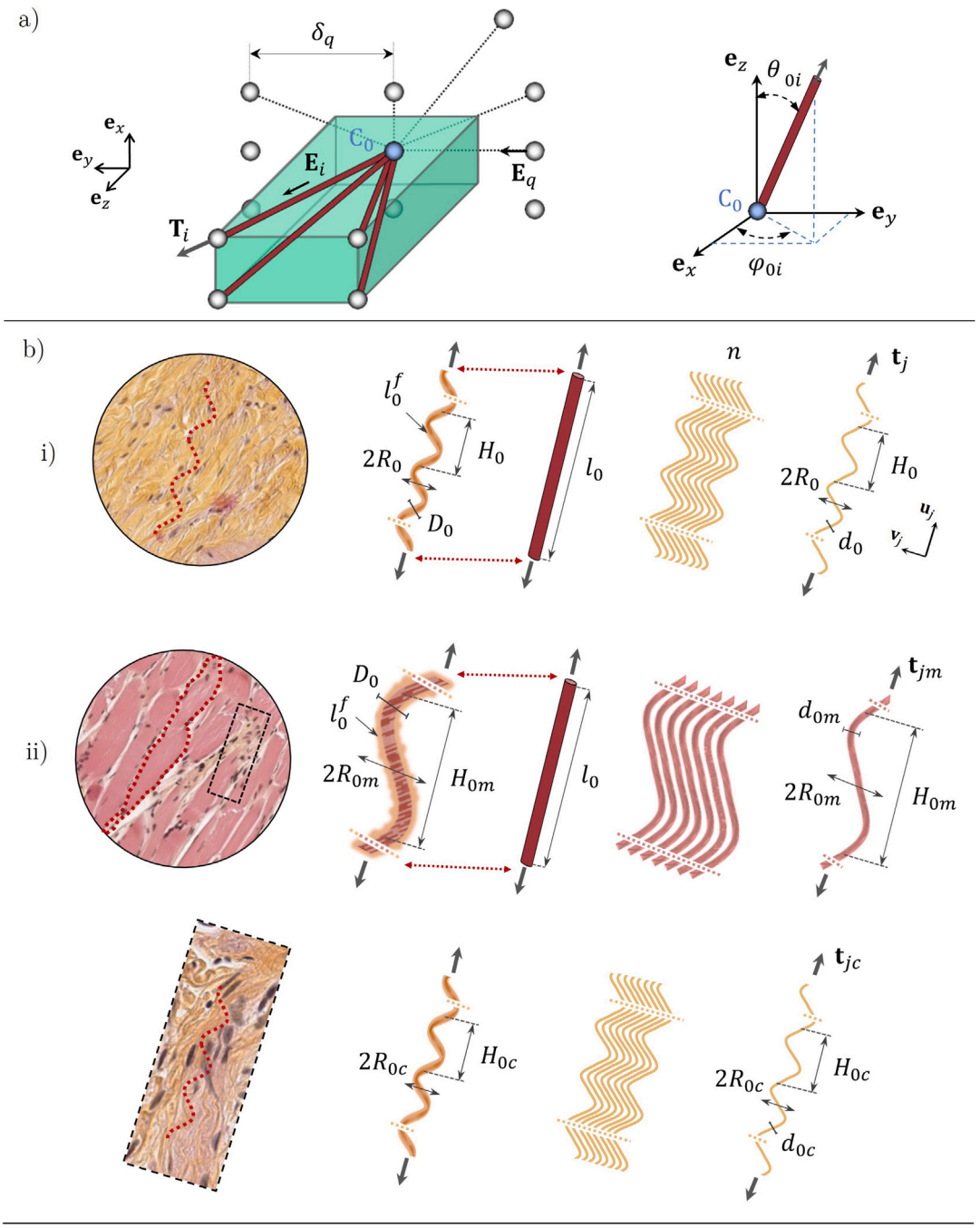

Fig. 2. Idealized geometry of the vocal-fold sublayers. (a) REV in the undeformed configuration $\mathcal{C}_0$: one node of periodicity C_0 (*blue*) and a 4-bar truss (*brown*) embedded in a soft isotropic matrix (*green*). The dotted lines illustrate the possible steric interactions of C_0 with the neighboring nodes. (b) Correspondence fiber-bar for (i) *lamina propria* and (ii) *vocalis*, conceived as fiber bundles of collagen (*orange*) and/or muscular fibrils (*pink*).

to take into account such steric interaction forces. More precisely, in the deformed configuration $\mathcal{C}$, once the relative distance δ_q between the two unconnected nodes C_0 and C_q ($q \neq 0$) exceeds a critical value δ_c, a repulsive force is activated to mimic the contact interactions between the concerned fibers. By periodicity, this comes to mimic the interactions between C_0 and its 5 neighboring nodes, as illustrated in Fig. 2(a) (see dotted lines). The resulting $M = 5$ fiber-to-fiber interaction forces are noted $\mathbf{R}_q$ and expressed using the power-law-based function (Rodney et al., 2005; Subramanian and Picu, 2011):

$$\mathbf{R}_q = R_q\,\mathbf{e}_q = \beta\, H(\varepsilon_q)\,\varepsilon_q^{\varsigma}\,\mathbf{e}_q \tag{6}$$

where $\varepsilon_q = \ln\left(\frac{\delta_q}{\delta_c}\right)$, $\mathbf{e}_q = \mathbf{c}_q\mathbf{c}_0/\|\mathbf{c}_q\mathbf{c}_0\|$, $H(.)$ is the Heaviside function, and where β and ς are interaction coefficients. Over small deformations and linear elasticity, ς should be equal to 2 in accordance with the Hertzian contact theory (Rodney et al., 2005; Subramanian and Picu, 2011). In the present study, dealing with hyperelastic bars and large transformations, ς was not fixed. A typical strain–repulsion force curve is shown in Fig. 3(b).

In the case of the *vocalis*, only one coefficient of interaction β and one length of interaction δ_c are defined for the two families of fibrils since steric interactions are considered at the fiber scale solely.

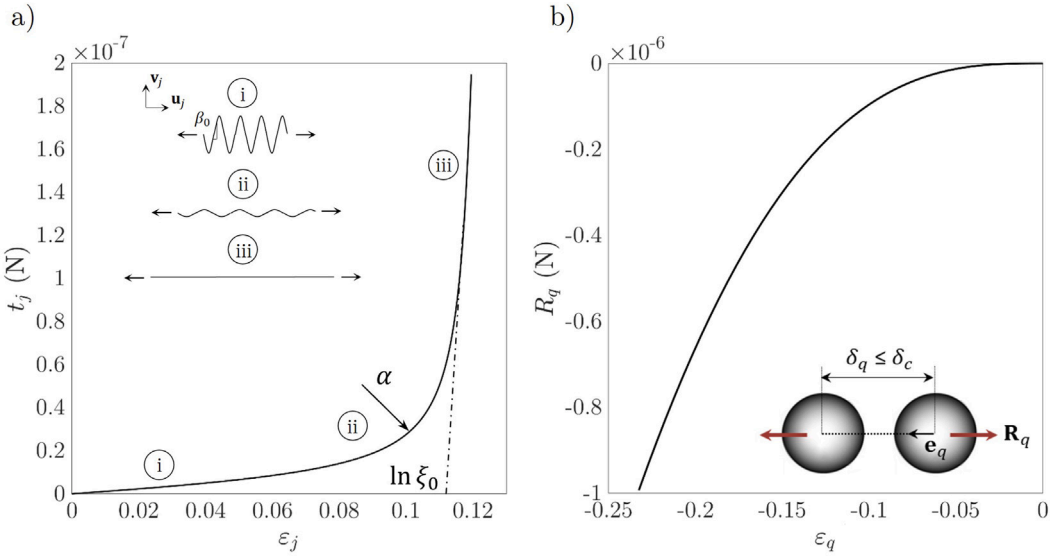

Fig. 3. (a) Strain–tension curve at the fibril scale. (b) Strain–repulsion force curve modeling fiber-to-fiber interactions.

2.4. Macro-mechanical behavior of the overall composites

Using the approach developed for aortic tissues (Bailly et al., 2012, 2014), the macroscale mechanical behavior of the *lamina propria* and the *vocalis* tissues can be determined. Regardless of the considered layer, its macroscopic Cauchy stress tensor $\boldsymbol{\sigma}$ is expressed as:

$$\boldsymbol{\sigma} = -p\boldsymbol{\delta} + \boldsymbol{\sigma}_m + \boldsymbol{\sigma}_f + \boldsymbol{\sigma}_s \tag{7}$$

where p is the incompressibility pressure, $\boldsymbol{\delta}$ the identity tensor, $\boldsymbol{\sigma}_m$ and $\boldsymbol{\sigma}_f$ represent the stress contribution of the matrix and the fibrous network, respectively, and where the stress contribution $\boldsymbol{\sigma}_s$ is induced by steric interactions.

Matrix – Under the previous assumptions, $\boldsymbol{\sigma}_m$ can be written as:

$$\boldsymbol{\sigma}_m = \mathbf{F} \cdot \left(\frac{\partial W}{\partial \mathbf{F}} \right)^T \tag{8}$$

Overall fibrous network – Using the homogenization method for trusses of hyperelastic bars (Caillerie et al., 2006), the bar $\boldsymbol{\sigma}_f$ and the steric $\boldsymbol{\sigma}_s$ tensors can be expressed as:

$$\boldsymbol{\sigma}_f = \frac{1}{V_{REV}} \sum_{i=1}^{N} \mathbf{T}_i \otimes \ell_i \mathbf{e}_i = \frac{\boldsymbol{\Phi}}{\pi d_0^2 \xi_0} \sum_{i=1}^{N} t_i \lambda_i \, \mathbf{e}_i \otimes \mathbf{e}_i \tag{9}$$

and

$$\boldsymbol{\sigma}_s = \frac{\boldsymbol{\Phi}}{\pi d_0^2 \xi_0} \sum_{q=1}^{M} R_q \delta_q^* \, \mathbf{e}_q \otimes \mathbf{e}_q \tag{10}$$

for the *lamina propria*, with $\lambda_i = \frac{\ell_i}{\ell_0}$ and $\delta_q^* = \delta_q / \ell_0$, and:

$$\boldsymbol{\sigma}_f = \frac{\boldsymbol{\Phi}_c}{\pi d_{0c}^2 \xi_{0c}} \sum_{i=1}^{N} t_{ic} \lambda_i \, \mathbf{e}_i \otimes \mathbf{e}_i + \frac{\boldsymbol{\Phi}_m}{\pi d_{0m}^2 \xi_{0m}} \sum_{i=1}^{N} t_{im} \lambda_i \, \mathbf{e}_i \otimes \mathbf{e}_i \tag{11}$$

and

$$\boldsymbol{\sigma}_s = \left(\frac{\boldsymbol{\Phi}_c}{\pi d_{0c}^2 \xi_{0c}} + \frac{\boldsymbol{\Phi}_m}{\pi d_{0m}^2 \xi_{0m}} \right) \sum_{q=1}^{M} R_q \delta_q^* \, \mathbf{e}_q \otimes \mathbf{e}_q \tag{12}$$

for the *vocalis*. Thus, the overall response of the *lamina propria* (resp. *vocalis*) depends on 12 (resp. 18) input parameters to be determined at rest:

6 (resp. 10) histological parameters: the fibrils diameter d_0 (resp. d_{0k}), their waviness amplitude R_0 (resp. R_{0k}), spatial periodicity H_0 (resp. H_{0k}) from which the tortuosity ξ_0 (resp. ξ_{0k}) can be estimated, the fibrils volume fraction $\boldsymbol{\Phi}$ (resp. $\boldsymbol{\Phi}_k$) and initial 3D fiber orientation (θ_0 , φ_0).

6 (resp. 8) mechanical parameters: the fibrils Young's modulus E_f (resp. E_{fk}), the matrix shear modulus μ, the transition parameter α (resp. α_k) and the interaction coefficients β, ς and δ_c related to the steric effects.

3. Model identification

The identification of the histo-mechanical parameters of the model was performed by adjusting its predictions to biomechanical data recently acquired on human vocal-fold tissues (Cochereau et al., 2020). To do so, a representative set of *lamina propria* and *vocalis* sublayers (hereinafter noted as LP_i and V_i, $i \in [1, 2]$) was selected from the reported database. Each sample was sequentially subjected to a series of finite-strain and cyclic physiological loadings, *i.e.,* longitudinal tension, transverse compression, and longitudinal shear. Only the first load–unload sequence of each test was considered, as displayed in Fig. 4 for samples (LP_1 , V_1), and Supplementary Fig. S1 for samples (LP_2 , V_2).

3.1. Simulated mechanical tests

To reproduce each experimental loading path, the REVs were subjected to the following loading conditions:

- Simple tension along the longitudinal direction $\mathbf{e}_z$ of the vocal folds, *i.e.,* with $\mathbf{F} = F_{xx}\,\mathbf{e}_x \otimes \mathbf{e}_x + F_{yy}\,\mathbf{e}_y \otimes \mathbf{e}_y + F_{zz}\,\mathbf{e}_z \otimes \mathbf{e}_z$ and $\boldsymbol{\sigma} = \sigma_{zz}\,\mathbf{e}_z \otimes \mathbf{e}_z$. The component F_{zz} was controlled, whereas F_{yy} was computed to ensure the transverse stress-free state condition $\sigma_{xx} = \sigma_{yy} = 0$. The component $F_{xx} = 1/F_{yy}F_{zz}$ was determined by the incompressibility condition. The hybrid conditions also allowed the pressure p to be determined.
- A similar procedure was employed for simple compression along the transverse direction $\mathbf{e}_x$.
- To simulate simple shear in the "longitudinal" plane ($\mathbf{e}_z, \mathbf{e}_x$), the REVs were subjected to $\mathbf{F} = \boldsymbol{\delta} + \gamma_{zx}\,\mathbf{e}_z \otimes \mathbf{e}_x$ and $p = 0$, where γ_{zx} is the imposed shear strain.

Regardless of the loading path, the stress predictions of the model were expressed using the first Piola–Kirchhoff stress tensor $\mathbf{P} = \boldsymbol{\sigma} \cdot \mathbf{F}^{-T}$.

Table 1
Set of histological parameters identified for *lamina propria* samples, LP_i. Gray-colored columns refer to quantities computed as a function of the determined histological parameters.

Sample	θ_0 (°)	φ_0 (°)	H_0 (μm)	R_0 (μm)	d_0 (μm)	Φ	ξ_0
LP_1	16	83	42	5	0.4	0.46	1.129
LP_2	16	83	42.5	5	0.4	0.48	1.126

Table 2
Set of mechanical parameters identified for *lamina propria* samples, LP_i.

Sample	E_f (MPa)	μ (Pa)	α	β (N)	ς	δ_c (μm)
LP_1	847	330	$4.4\ 10^{-3}$	$2\ 10^{-4}$	3	66
LP_2	847	290	$4.3\ 10^{-3}$	$4\ 10^{-4}$	3	65.7

3.2. Optimization procedure

In order to fit macroscale stress–strain responses, the following protocol was adopted to obtain optimized sets of histo-mechanical parameters:

(i) As far as possible, all input histological parameters were determined from microstructural analyses collected on the unloaded samples and observed using 2D standard optical microscopy (Cochereau et al., 2020). Alternatively, the remaining histo-mechanical parameters were initialized and bounded within a range of physiological values determined from the literature.

(ii) A least-squared approach was used to minimize the discrepancies between theoretical and experimental stress tensors. To do so, a nonlinear constraint optimization process was applied, as in Bailly et al. (2012). For each tested sample, this procedure accounts for the three mechanical loading conditions the sample was subjected to. Furthermore, as the proposed model is purely hyperelastic, it cannot reproduce the hysteresis observed experimentally (Cochereau et al., 2020). The optimization procedure was accordingly adjusted to experimental "neutral" stress–strain curves, lying in between the loading and unloading paths.

4. Results and discussion

4.1. Histo-mechanical parameters: choice of initial guesses and optimized values

In order to obtain the optimized histological parameters reported in Tables 1 and 2 for the *lamina propria* samples and in Tables 3 and 4 for the *vocalis* ones, initial guess corridors discussed hereafter were initially used.

4.1.1. Lamina propria

Collagen volume fraction Φ: According to the literature, Φ is reported to vary between 0.15 and 0.55 depending on the tissue depth $\mathbf{e}_x$ (Bühler et al., 2011; Hahn et al., 2006b; Miri et al., 2013; Tateya et al., 2006). Note that the upper limit may appear underestimated when analyzing the micrographs of the chosen samples LP_i zoomed in their deepest sublayers (Fig. 1), but it is relevant when averaged over the whole sample thickness. Within this range of admissible values, the optimization led to $\Phi \approx 0.47$ for both LP_i samples.

Collagen fibril's diameter d_0: d_0 is known to range between 10 nm (collagen Type III) and 500 nm (Type I) (Asgari et al., 2017; Fratzl, 2008; Gautieri et al., 2012; Gelse et al., 2003; Yang et al., 2008). By imposing these physiological boundaries, the identification procedure conducted to $d_0 = 400$ nm for each sample.

Fibril's sine waveform parameters (H_0; R_0): The spatial period and amplitude of wavy collagen fibrils at rest were bounded within the corridors (10–70 μm; 1–10 μm) respectively (Bailly et al., 2018; Miri et al., 2013). The optimization process led to similar values for both samples, close to (42 μm; 5 μm), implying an initial tortuosity ξ_0 of about 1.13.

Network 3D orientation (θ_0; φ_0): The 3D angular distribution of collagen fibrils in the *lamina propria* was extrapolated from recent 3D CT images obtained on a single unloaded sample (Bailly et al., 2018) for which (θ_0; φ_0) = (30°; 39°), showing a pronounced preferred orientation along $\mathbf{e}_z$ and a slight orthotropy in the perpendicular plane. To account for the inter-sample variability, previous values were let free to vary within the range (0–50°; 20–90°). The optimization process led to (θ_0; φ_0) ≈ (16°; 83°) for both samples, a nearly 2D network in the plane ($\mathbf{e}_z$, $\mathbf{e}_y$). It should be noticed that a quasi-plane network (*i.e.,* $\theta_0 \leq 35°$ and $\varphi_0 \geq 80°$) was required by the model to properly reproduce the *lamina propria*'s shear response.

Collagen fibril's Young modulus E_f: Although very challenging, the mechanical properties of a single collagen (Type I) fibril have already been investigated using Atomic Force Microscopy, Micro Electro Mechanical Systems technology and X-ray diffraction (Buehler, 2008; Gautieri et al., 2012; Lorenzo and Caffarena, 2005; Shen et al., 2008; Yang et al., 2008). In aqueous media, the tangent modulus measured in longitudinal tension, E_f, is ranging from 1 MPa at small strains up to an asymptotic value of 1 GPa at finite strains, where a linear stress–strain regime is achieved. Imposing these boundaries, the optimization process yielded to $E_f \approx 850$ MPa for both LP_i samples.

Matrix shear modulus μ: This parameter was first initialized by the shear modulus of hyaluronic acid $\mu_{HA} \approx$ 20–50 Pa (Heris et al., 2012), *i.e.,* the major and most abundant component of the ground substance within the *lamina propria* (Chan et al., 2001; Finck and Lefebvre, 2005; Finck, 2008; Finck et al., 2010; Gray et al., 1999; Hahn et al., 2006a; Hammond et al., 1997; Heris et al., 2012). In order to account for other components within the matrix (*e.g.,* cells, elastin), μ was let free to vary up to 1.5 MPa, *i.e.,* the estimated Young's modulus of isolated elastin fibers (Yang, 2008; Yang et al., 2008). The optimization finally yielded to $\mu \approx \mathcal{O}(10^2)$ Pa for both samples.

Transition parameter α: Initially not fixed, the optimization yielded to $\alpha \approx \mathcal{O}(10^{-3})$ for both samples. This order of magnitude was further confirmed by comparing the tension t_j predicted by the micro-mechanical model when a fibril (d_0, H_0, R_0, E_f) is stretched to that predicted by the FE simulation (not shown here) of the stretching of a corrugated elastic beam with identical properties.

Interaction coefficient β, ς and δ_c: β, ς and δ_c were freely adjusted during the optimization process, respectively yielding to $\approx \mathcal{O}(10^{-4})$ N, ≈ 3 and ≈ 66 μm for both samples. To our knowledge, contact forces endured by entangled collagen fibers in soft living tissues are not documented. This is probably ascribable to experimental limitations. However, the reaction forces determined on collagen fibrils using transverse nano-indentation were recently reported (Asgari et al., 2017), showing an amplitude of $\mathcal{O}(10^2)$ pN, *i.e.,* of the same order of magnitude of the

Table 3
Set of histological parameters identified for *vocalis* samples, V_i. $k \in \{c, m\}$ labels collagen or muscular fibrils accordingly. Gray-colored columns refer to quantities computed as a function of the determined histological parameters.

Sample	θ_0 (°)	φ_0 (°)	H_{0k} (μm)	R_{0k} (μm)	d_{0k} (μm)	Φ_k	ξ_{0k}
V_{1_c}	33	70	28	6.4	0.4	0.10	1.4
V_{1_m}	33	70	1350	130	1	0.70	1.08
V_{2_c}	28	67	30	5.5	0.4	0.12	1.28
V_{2_m}	28	67	1620	90	1	0.70	1.03

Table 4
Set of mechanical parameters identified for *vocalis* samples V_i. $k \in \{c, m\}$ labels collagen or muscular fibrils accordingly.

Sample	E_{fk} (MPa)	μ (Pa)	α_k	β (N)	ς	δ_c (μm)
V_{1_c}	847	900	$4.4\ 10^{-3}$	$2.2\ 10^{-4}$	3	367
V_{1_m}	0.05	900	$1.1\ 10^{-2}$	$2.2\ 10^{-4}$	3	367
V_{2_c}	847	980	$4.4\ 10^{-3}$	$7.6\ 10^{-5}$	3	360
V_{2_m}	0.05	980	$2.7\ 10^{-2}$	$7.6\ 10^{-5}$	3	360

predicted reaction forces R_q between fibers during transverse compression (see Fig. 6). It is also worth noting that interaction lengths δ_c remain rather close to the fiber's characteristic "encumbrance", *i.e.,* $\mathcal{O}(2R_0+D_0)$, where typical values of the collagen fiber bundle diameter D_0 range between 1 and 20 μm (Borg and Caulfield, 1980; Fratzl, 2008).

4.1.2. Vocalis

For collagen sheaths, the parameters d_{0c}, E_{fc}, α_c were respectively set equal to the optimized values d_0, E_f, α previously obtained for the *lamina propria* (see Tables 1 and 2). Furthermore, the equivalent myofibrils diameter was set to $d_{0m} = 1$ μm which is in agreement with measurements performed on V_i micrographs (Cochereau et al., 2020) and with other available data (Sato and Tauchi, 1982; Colomo et al., 1997; Lieber, 1986; Mukund and Subramaniam, 2020; Chen et al., 2006; Bailly et al., 2018).

Volume fractions Φ_k: Consistently with the values measured for the considered samples (Cochereau et al., 2020), myofibrils' (resp. collagen fibrils') volume fraction Φ_m (resp. Φ_c) in the *vocalis* were found within the range 0.60 to 0.80 (resp. 0.05 to 0.15). If little is reported regarding Φ_m for skeletal muscles, our measurements for Φ_c seem consistent with other values collected on rabbit tissues (Ward et al., 2020), varying from 0.10 to 0.25. Therefrom, within these ranges of admissible values, the optimization led to $\Phi_m \approx 0.70$ (resp. $\Phi_c \approx 0.10$) for both V_i samples.

Muscular and collagen fibril's sine waveform parameters(H_{0k};R_{0k}): Spatial period and amplitude of wavy myofibrils (H_{0m}; R_{0m}) were bounded within narrow corridors (1300–1700 μm; 70–140 μm) (Bailly et al., 2018). The optimization procedure led to distinct values for V_i samples, yielding to tortuosity ξ_0 of 1.08 and 1.03 respectively, showing rather straight fibrils at rest in both cases in accordance with Fig. 1. Regarding collagen fibrils' tortuosity, physiological bounds were kept as set in *lamina propria*, which yielded to (H_{0c}; R_{0c}) ≈ (30 μm; 6 μm) after optimization. Thus, the model identification suggests that collagen fibrils covering each myofibrils bundle in the *vocalis* at rest are wavier that those laying in the *lamina propria* (from 15 up to 23 %). This result is in agreement with previous micrographs, showing a double wavelength for the collagen sheath, due to a first muscular waviness entwined with a second-degree collagen crimping.

Network 3D orientation (θ_0; φ_0): As for the *lamina propria*-case, initial orientation of the muscular network was determined extrapolating 3D descriptors from *vocalis* X-ray images (Bailly et al., 2018), *i.e.,* (θ_0; φ_0) ≈ (33°; 53°). Final model identification led to (θ_0; φ_0) ≈ (30°; 68°) for both samples.

Myofibril's Young modulus E_{fm}: The "passive" longitudinal Young modulus of frog and rabbit myofibrils (Magid and Law, 1985; Ward et al., 2020) is reported to range from 1 to 35 kPa below 10% strains, rising up to ≈60 kPa at finite strains. Within this range of admissible values, the optimization process yielded to $E_{fm} \approx 50$ kPa for both V_i samples.

Matrix shear modulus μ: *Vocalis* ground substance composition was assumed to be close to that of the *lamina propria*. Accordingly, *vocalis* matrix shear modulus μ was calibrated on HA data, as detailed for the *lamina propria*-case. This conducted to $\mu \approx \mathcal{O}(10^3)$ Pa for both samples.

Parameter α_m: Optimization yielded to $\alpha_m \approx \mathcal{O}(10^{-2})$ for both samples.

Interaction coefficient β, ς and δ_c: As for the *lamina propria*-case, no constraints were applied to the three parameters during the model identification, yielding to values of $\beta \approx \mathcal{O}(10^{-4})$ and $\mathcal{O}(10^{-5})$ N for each V_i sample, $\varsigma \approx 3$ and $\delta_c \approx 360$ μm for both samples.

4.2. Macro and microscale predictions

A comparison between the model macroscale predictions and corresponding experimental data acquired is illustrated in Fig. 4, for both sublayers (LP_1 and V_1 – results obtained for LP_2 and V_2 are reported in Fig. S1, Appendix A) and for three loading modes, *i.e.,* tension, compression, shear. For each case, the stress–strain response of a homogeneous isotropic neo-hookean material with the same mechanical properties of the corresponding matrix was superimposed to better understand the contribution of each phase to the overall composite behavior. The strain-induced evolution of microscale descriptors is displayed in Figs. 5 and 6.

- *Longitudinal tension* – Regarding the *lamina propria*, the model fairly well captures its macroscale nonlinear stress–strain response with a typical J-shape strain-hardening (Fig. 4a). The stress contribution predicted for the matrix-equivalent medium is negligible compared to the overall response of the composite sublayer. This emphasizes the major mechanical role of the collagen fibrous network to the longitudinal tensile behavior of the *lamina propria*, which is supported by predictions of lower-scale mechanisms: as shown in Fig. 5a, collagen fibrils are permanently stretched during the load, and gradually unfolded. The tensile response is coupled with a noticeable rotation and progressive alignment towards the load direction $\mathbf{e}_z$, so that angles θ_i decrease down to 10° at $\varepsilon_{zz} \approx 0.10$. These micro-mechanisms result in large deformations of the REV, highly stretched along $\mathbf{e}_z$, shrunk along $\mathbf{e}_y$ (*e.g.,* with $\varepsilon_{yy} \approx -0.60$ for LP_1 at $\varepsilon_{zz} = 0.10$), but also expanded along $\mathbf{e}_x$ (*e.g.,* with $\varepsilon_{xx} \approx 0.50$), thereby exhibiting an auxetic behavior. Conversely, these transverse deformations would be close to $\varepsilon_{yy} = \varepsilon_{xx} \approx -0.05$ without any fibers ($\Phi = 0$), *i.e.,* with an incompressible isotropic material (see Fig. 5a, *in green*). The predicted auxeticity of the *lamina propria* is ascribable to a strong coupling between the high anisotropy of its collagen network and the incompressibility constraint.
  Concerning the *vocalis*, the macroscale tensile behavior is similarly rather well predicted by the model (Fig. 4a), whereas the involved micro-mechanisms slightly differ due to histo-mechanical

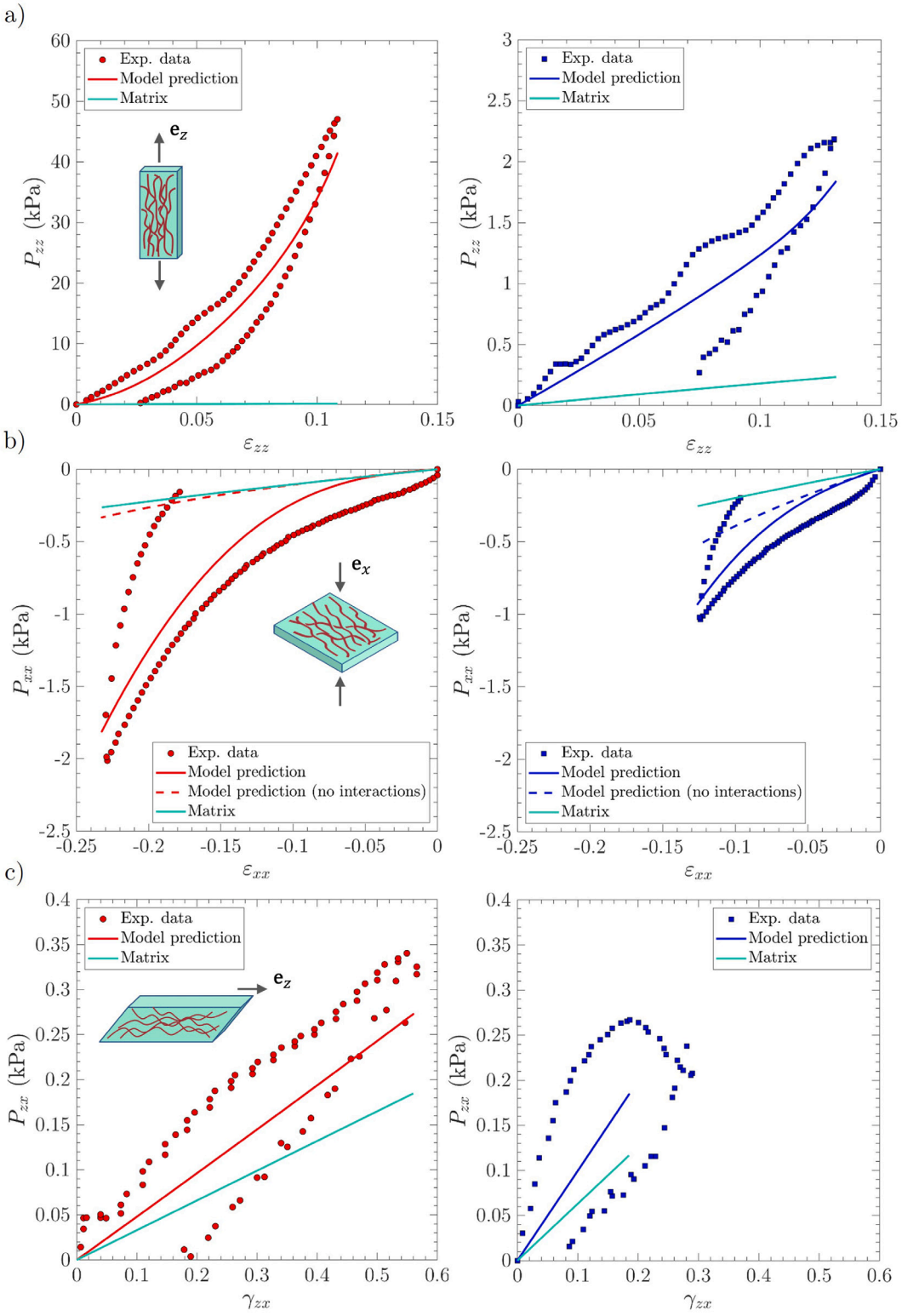

Fig. 4. Macroscopic stress–strain curves of vocal-fold sublayers under multiaxial loadings. Experimental data *vs.* model predictions obtained for *lamina propria* sample LP_1 (*left*, in red) and *vocalis* sample V_1 (*right*, in blue): (a) longitudinal tension, (b) transverse compression, (c) longitudinal shear.

discrepancies between the tissues. The less pronounced nonlinear response of the *vocalis* is attributable both to a lower initial tortuosity ξ_0 and to the negligible stiffness of muscular fibers compared to that of collagen fibers. Note that Fig. 5b shows the key role played by the sheaths of collagen fibers surrounding muscle fibers, as recently reported by Ward et al. (2020), in the definition of the tissue passive tensile properties. Still, a minor volume fraction of collagen leads to lower orders of magnitude stress levels at the macroscale, compared to those displayed by the *lamina propria*.

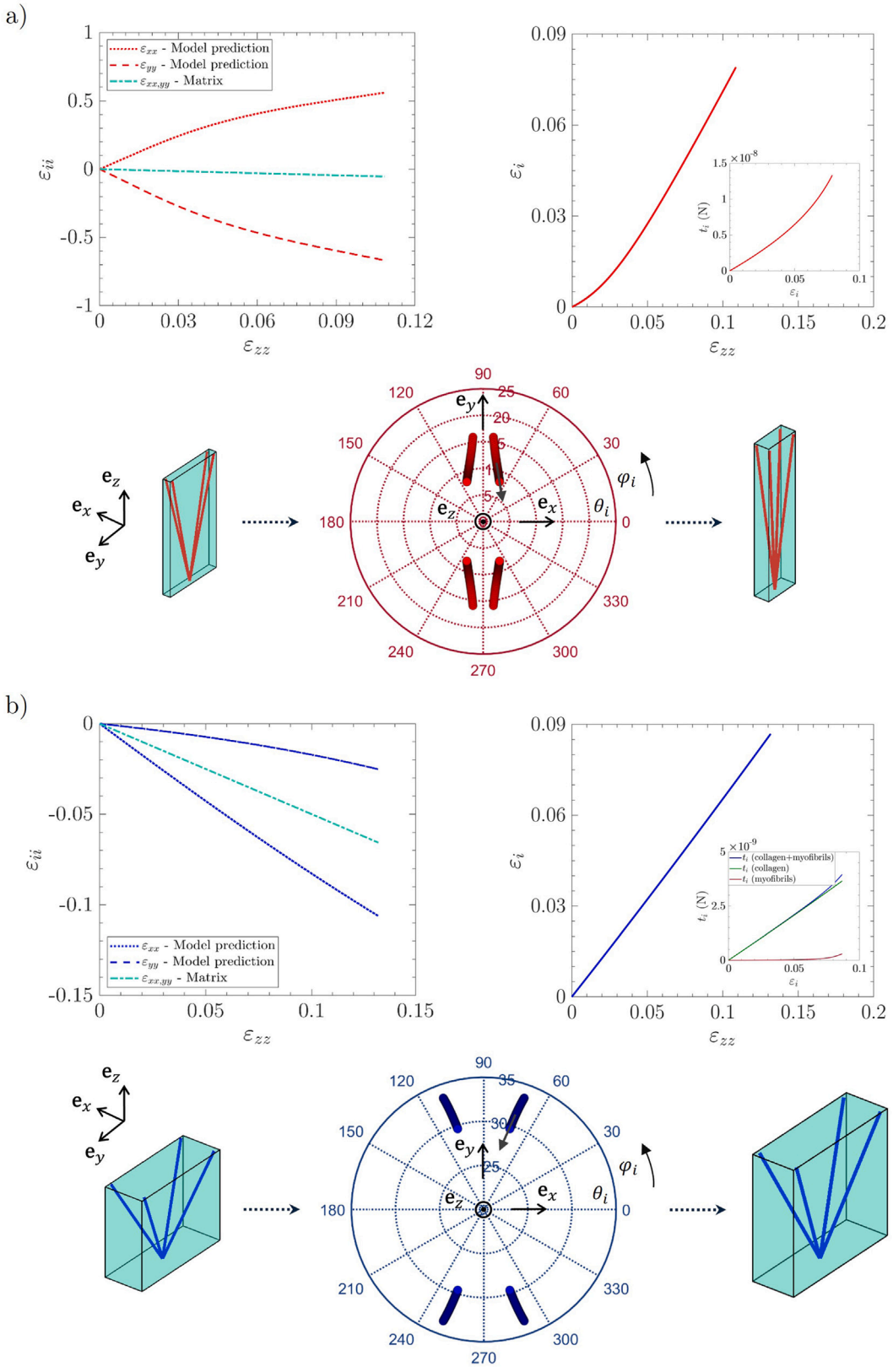

Fig. 5. Strain-induced evolution of multiscale descriptors predicted for (a) *lamina propria* LP_1, and (b) *vocalis* V_1 during tension along $\mathbf{e}_z$: *(top left)* macroscopic loading paths; *(bottom)* stereographic projection of orientation vectors $\mathbf{e}_i$ from initial to final state, $i \in [1..4]$; *(top right)* strain-variation of the fibril chord ϵ_i, and corresponding tension t_i.

- *Transverse compression* – The nonlinear response and strain hardening of the *lamina propria* is additionally well reproduced under transverse compression along $\mathbf{e}_x$, *i.e.,* applied perpendicularly to the main fiber orientation. However, in this case, the macroscale nonlinearity is not inherited from the coupled unfolding/rotation of the collageneous network: indeed, Fig. 6a shows that the fibrils'

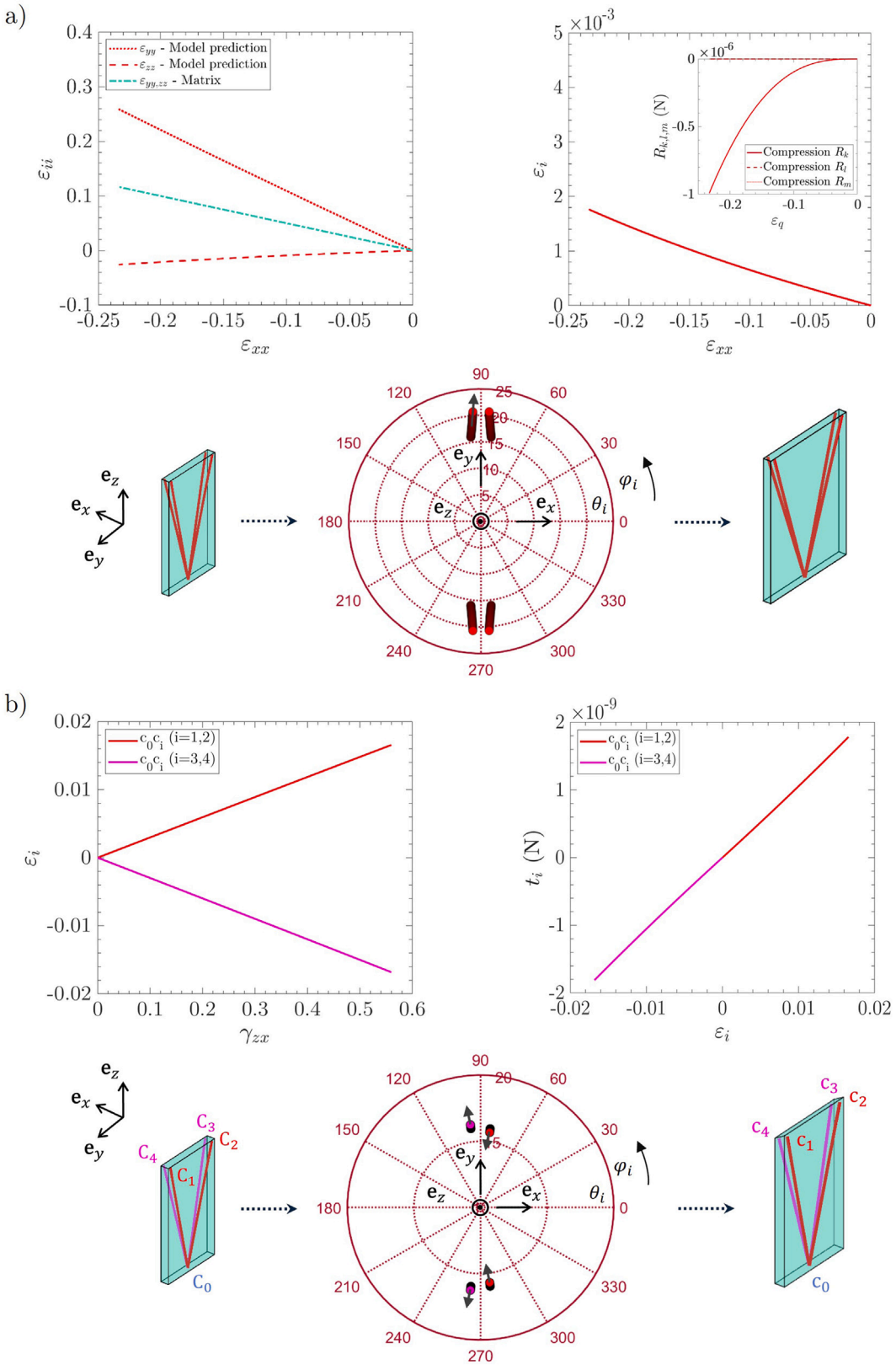

Fig. 6. Strain-induced evolution of multiscale descriptors for *lamina propria* LP_1 during (a) compression along $\mathbf{e}_x$ and (b) shear in the plane ($\mathbf{e}_z$, $\mathbf{e}_x$). (a) Compression case: *(top left)* macroscopic loading paths; *(bottom)* stereographic projection of orientation vectors $\mathbf{e}_i$ from initial to final state, $i \in [1..4]$; *(top right)* strain-variation of the fibril chord ε_i and interaction forces R_q. (b) Shear case: *(top left)* strain-variation of the fibril chord ε_i; *(top right)* corresponding tension t_i; *(bottom)* same as in (a).

end-to-ends are barely stretched ($\forall\ \varepsilon_{xx}$, $\varepsilon_i \approx 0$, $t_i \approx 0$ and $\xi_i \approx \xi_0$). Fibers rotations in the ($\mathbf{e}_y$, $\mathbf{e}_z$) plane are also moderate, *e.g.*, angles θ_i (resp. φ_i) of about 5° (resp. 2°) at $\varepsilon_{xx} \approx -0.25$. Auxetic effects along the $\mathbf{e}_z$-direction are still predicted, albeit less

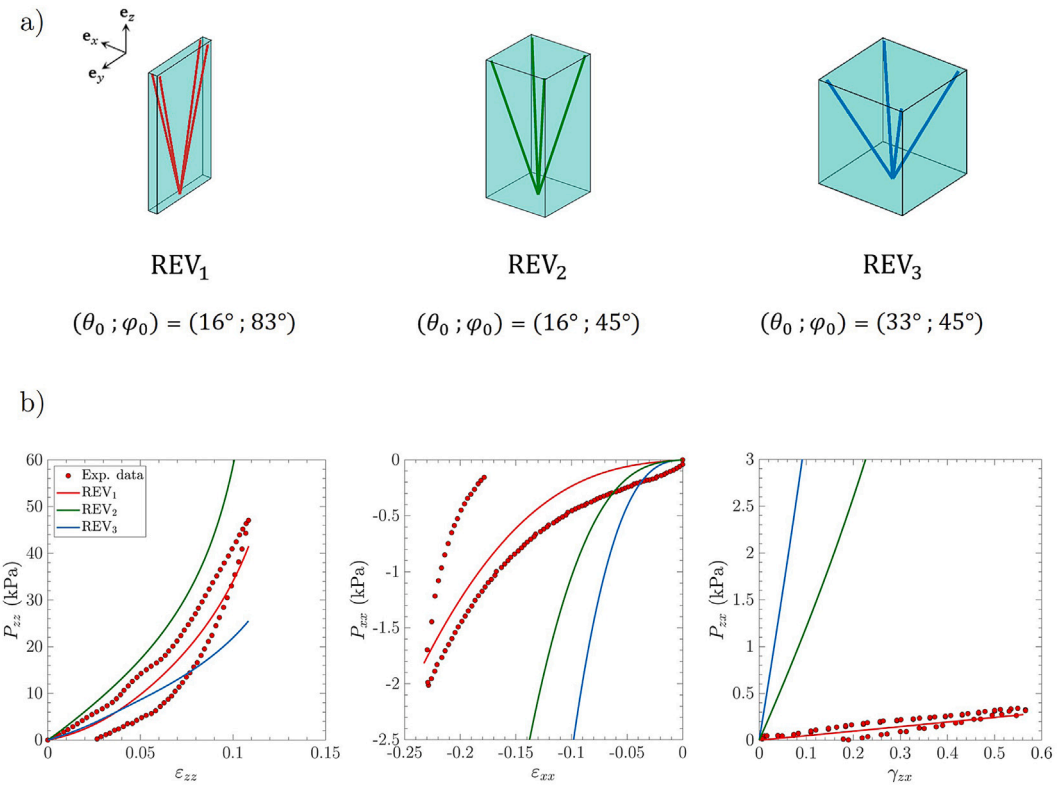

Fig. 7. (a) Panel of the three REVs in the undeformed configuration $\mathcal{C}_0$, proposed to gauge the effect of 3D fiber orientations on the *lamina propria* mechanics. (b) Predicted stress–strain responses obtained for each REV subjected to longitudinal tension, transverse compression and longitudinal shear (*from left to right*), along with reference experimental data (LP$_1$).

marked than in longitudinal tension. The origin of the nonlinearity exhibited at the tissue scale should rather be sought in the steric interactions: Fig. 6a shows non-zero microscopic repulsion forces R_k predicted along the load direction, while interaction forces in other $\mathbf{e}_q$-directions (see Fig. 2) – here noted R_l and R_m – are not triggered. More generally, among all the modeling cases considered in the present study, steric interactions were activated under compressive loading exclusively. Furthermore, Fig. 4b displays what macroscale predictions would be when neglecting steric hindrance effects ($\beta = 0$, see dotted lines), showing a quasi-linear mechanical behavior very close to that of the matrix. By contrast with the trends obtained in longitudinal tension, this highlights the major mechanical contribution of the matrix under compression at low strains, and its strong attenuation once steric interactions are triggered (for $\varepsilon_{xx} \approx -0.05$). Similar results are obtained for *vocalis* sample V$_1$, even though a faster fiber recruitment and unfolding are predicted in that case.

- *Longitudinal shear* – Leaving aside the experimental artifacts at the end of the load (notably for the *vocalis*) (Cochereau et al., 2020), the model yields to rather good theoretical predictions of both sublayers' shear responses, capturing the quasi-constant strain hardening exhibited in Fig. 4c. The predicted mechanical behavior is very close to that of the sole matrix. This is ascribable to the mechanisms evidenced at the microscale and illustrated in Fig. 6b for LP$_1$: fibers rotation is negligible, and their unfolding is limited. More specifically, fibers $i = \{1,2\}$ are slightly stretched, while fibers $i = \{3,4\}$ are compressed ($\forall i$, $|\varepsilon_i| < 0.02$) so that they all remain crimped during the load — the complete unfolding of the fibers being predicted for $\gamma_{zx} \approx 3$.

4.3. Effect of fiber orientation on the monotonic and vibratory properties

The identified model is used in this section to further investigate the effect of fiber orientation on the mechanics of the *lamina propria*, subjected both to quasi-static monotonic and vibratory loading. More specifically, a major focus was drawn to the degree of alignment and symmetry along the antero-posterior direction $\mathbf{e}_z$ by studying the mechanics of REVs owning identical histo-mechanical properties (see Tables 1 and 2), albeit different initial fiber orientations (θ_0; φ_0). As illustrated in Fig. 7a, three distinct 3D configurations were selected, differentiated two-by-two by a single angular parameter: (i) a first reference quasi-planar and highly oriented orthotropic structure REV$_1$, resulting from the previous model identification (sample LP$_1$); (ii) a second configuration with a high orthotropic fiber orientation along $\mathbf{e}_z$, albeit equilibrated (*i.e.,* with in-plane tetratropy in the ($\mathbf{e}_x$, $\mathbf{e}_y$) plane simulating highly oriented fibrous structures but with transverse isotropy), noted REV$_2$ — this configuration corresponds to LP$_1$ optimal set of histo-mechanical parameters but $\varphi_0 = 45°$; (iii) a third equilibrated structure with a moderate fiber alignment along $\mathbf{e}_z$, noted REV$_3$ – this last configuration is less orientated than REV$_2$ and tends toward the rotational symmetry of the antero-posterior axis, being a standard assumption to model vocal-fold tissues so far (*e.g.,* Berry and Titze, 1996; Kelleher et al., 2013b; Weiß et al., 2013).

- *Monotonic loading* – The predicted stress–strain curves in longitudinal tension, transverse compression and longitudinal shear for the three structures are compared in Fig. 7b. Globally, strongly oriented structures exhibit stiffer responses in longitudinal tension, whereas less oriented configurations offer a higher resistance in longitudinal shear and transverse compression. In particular, comparing the responses of REV$_1$ and REV$_2$ allows to estimate the impact of the microstructural symmetry: despite very close θ_0-values, their multiaxial responses differ drastically.

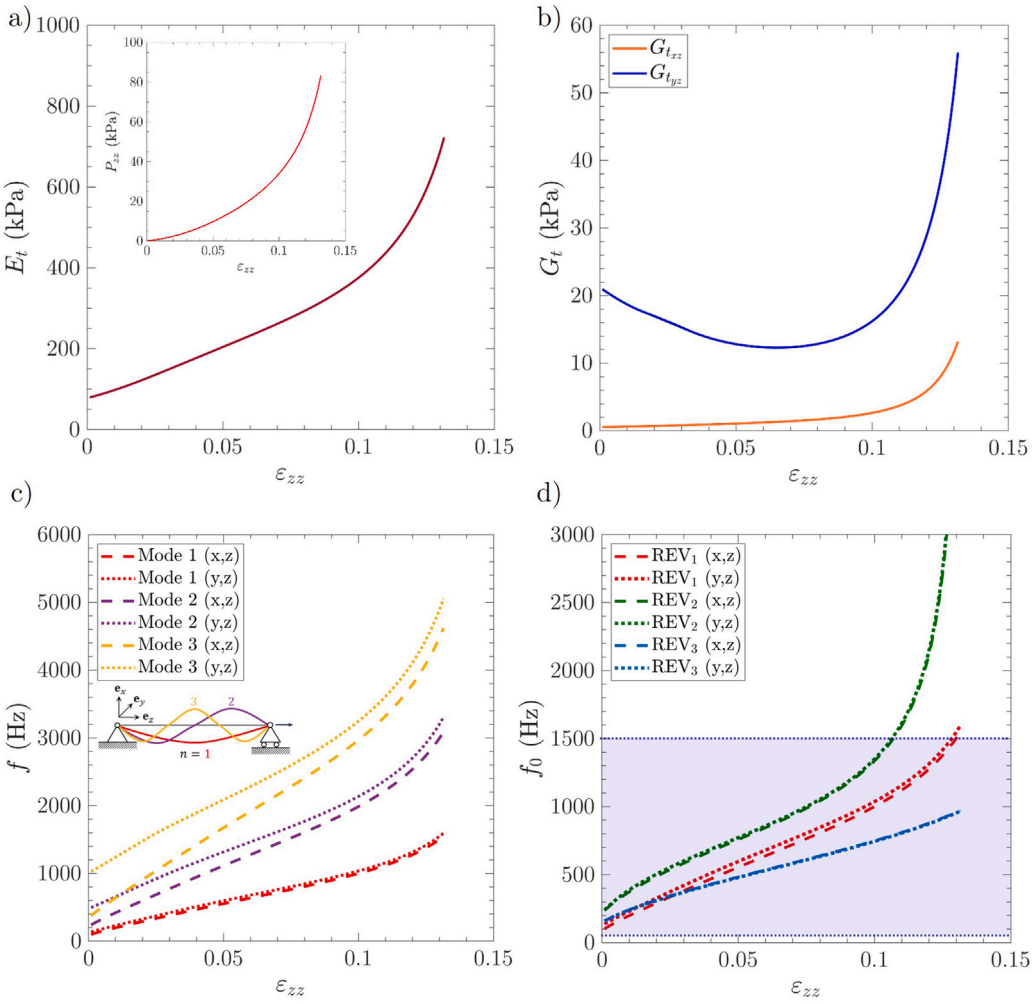

Fig. 8. Theoretical predictions of *lamina propria*'s vibratory properties as functions of the applied tensile strain ε_{zz}. (a) Tangent longitudinal modulus E_t, as derived from the predicted nominal stress P_{zz} (REV$_1$, see inset). (b) Tangent transverse shear moduli $G_{t_{xz}}$ and $G_{t_{yz}}$ (REV$_1$). (c) First three modal frequencies in the $(\mathbf{e}_x, \mathbf{e}_z)$ and $(\mathbf{e}_y, \mathbf{e}_z)$-planes of vibration (REV$_1$). (d) Fundamental frequency f_0 obtained for the three structures REV$_1$, REV$_2$ and REV$_3$. Blue-shaded area: human voice f_0 range.

In tension, structure REV$_1$ shows lower stress levels and tangent moduli: the structure is required to open along $\mathbf{e}_x$ before enabling fibers to work in tension along $\mathbf{e}_z$. Conversely, a transverse isotropic structure limits fibers' rotation along the load direction, thus leading to an earlier fiber recruitment, which stiffens the macroscopic tissue response (see Supplementary Videos V1, V2 and V3 in Appendix A). Likewise, the response of REV$_1$ is softer in compression: the contraction and repulsive forces due to steric hindrance along $\mathbf{e}_x$ being induced after sufficient in-plane rotations of fibers and global opening of the structure along $\mathbf{e}_y$ (see Supplementary Videos). Similar qualitative trends are exhibited in shear, even if the fiber rotation is negligible in this case: fiber recruitment is faster for REV$_2$, inducing higher stress levels at the macroscale (see Supplementary Videos). In conclusion, a rather small change in the initial orientation of the fibrous network may result in a combination of nonlinear micro-mechanisms of deformation (*e.g.,* fibers' rotations, uncrimping, tension, compression and steric interactions), which in turn would strongly impact the multiaxial behavior of the *lamina propria*. Finally, this study points out that a orthotropic configuration is more suited than a transverse isotropic structure to reproduce the physiological loading conditions the *lamina propria* is subjected to *in vivo*.

- *Vibratory loading* – To better highlight the impact of these fiber-scale micro-mechanisms on vocal-fold vibrations, a simplified analysis of the *lamina propria* vibratory properties is here tackled resorting to beam theory. Various beam models are used in the literature to semi-quantitatively describe the vocal-fold vibration (Descout et al., 1980; Bickley, 1989; Titze and Hunter, 2004; Zhang et al., 2007, 2009), albeit with a poor correlation to the tissue's microstructural specifications. The approach proposed by Kelleher et al. (2013b) is here adopted using the present micro-mechanical model to compute the natural frequencies of the *lamina propria* subjected to transverse vibrations. Thus, as a first approximation, the *lamina propria* is considered as a pinned–pinned Timoshenko beam of rectangular cross-section (initial length L_0, width w_{0y}, thickness w_{0x}), with incompressible, anisotropic and hyperelastic properties. When subjected to a tensile strain ε_{zz} along the antero-posterior direction $\mathbf{e}_z$, the corresponding frequency of the n^{th} mode of vibration of the beam, noted f_n, can be expressed as follows (Kelleher et al., 2013b):

$$f_n(\varepsilon_{zz}) = \frac{n^2\pi^2}{L^2}\sqrt{\frac{E_t I}{\zeta \rho A}\left(1 + \frac{\vartheta L^2}{n^2\pi^2 E_t I} + \frac{\vartheta}{k_s G_t A}\right)}, \tag{13}$$

with

$$\zeta(\varepsilon_{zz}) = 1 + n^2\pi^2\left(\frac{I}{AL^2}\left(1 + \frac{\vartheta}{k_s G_t A}\right) + \frac{E_t I}{k_s G_t A L^2}\right), \tag{14}$$

and where $L = L_0\, e^{\epsilon_{zz}}$ is the beam length, $A = w_x w_y$ its cross-section ($w_x = w_{0x}\, e^{\epsilon_{xx}}$, $w_y = w_{0y}\, e^{\epsilon_{yy}}$), $\vartheta = A\,\sigma_{zz}$ the applied

longitudinal tension, ρ the tissue density, k_s the Timoshenko's shear correction coefficient ($k_s = 5/6$ for a beam of rectangular cross-section), and where E_t is the longitudinal tangent modulus predicted by the micro-mechanical model at ε_{zz} (see Fig. 8a in the case of REV_1). Accounting for the orthotropic properties of the *lamina propria*, two planes of vibration ($\mathbf{e}_x$, $\mathbf{e}_z$) and ($\mathbf{e}_y$, $\mathbf{e}_z$) were considered. The beam's second moment of inertia $I = w_x\, w_y^3/12$ (resp. $w_y\, w_x^3/12$) and its predicted tangent shear modulus $G_t = G_{t_{xz}}$ (resp. $G_{t_{yz}}$) were varied accordingly (see Fig. 8b in the case of REV_1). Choosing $\rho = 1040$ kg m^{-3}, $L_0 = 17$ mm and $w_{0x} = w_{0y} = 1.5$ mm (Cochereau et al., 2020; Kelleher et al., 2013b), natural frequencies of the first three modes of vibration ($n = 1..3$) were derived for REV_1 — the latter being expected to account for 99% of the energy at the onset of vocal-fold self-oscillation (Kelleher et al., 2013b). Corresponding predictions $f_1 < f_2 < f_3$ are displayed in Fig. 8c for both planes of vibration in the case of structure REV_1. They drastically increase with the applied pre-strain ε_{zz}, this being mainly ascribed to a stiffening of E_t (see Fig. 8a). Additionally, the marked orthotropy of REV_1 induces a significant difference for f_2 and f_3 depending on the vibration plane. Note that f_1 is also referred to as f_0, it being the expected acoustical fundamental frequency during phonation to a first approximation. Comparison of f_0 predictions for structures REV_1, REV_2 and REV_3 is analyzed in Fig. 8d. Regardless of the considered case, a nonlinear evolution of f_0 with the applied strain is observed for all frequencies, in quantitative agreement with typical *in vivo* f_0 data (50–1500 Hz) (Brown et al., 1991; Krook, 1988) and with former theoretical works based on the gold-standard Gasser–Ogden–Holzapfel constitutive model (Kelleher et al., 2013b; Gasser et al., 2006). More importantly, the induced effect of the initial fiber orientation on f_0 is clearly evidenced.

5. Conclusion

In this study we proposed an idealized description of the 3D fibrous architecture of human vocal-fold sublayers, *i.e.,* the *lamina propria* and the *vocalis*, based on histological evidence. Therefrom, a new 3D micro-mechanical model of vocal-fold tissues was proposed and identified on four experimental targets, *i.e.,* two *lamina propria* and two *vocalis* samples. From a single set of histo-mechanical parameters per sample, this model is able not only to reproduce its nonlinear and anisotropic behavior under key physiological loadings (tension, compression, shear), but also to predict the underlying deformation micro-mechanisms at the fiber scale *i.e.,* a complex and path-dependent combination of 3D fibers' rotations, matrix/fibers deformations and interactions that were analyzed to clarify the inherited macroscopic tendencies. More particularly, this study highlights the major role of 3D fiber orientation in longitudinal tension, steric hindrance in transverse compression and matrix contribution in longitudinal shear. We also showed that a slight change of the histo-mechanical configuration may drastically alter both the tissue monotonic and vibratory properties, which in turn would affect vocal folds vibration *in vivo*.

Further developments are needed to improve the proposed micro-mechanical model. Although challenging to identify experimentally, the introduction of microscale time-dependent phenomena would be needed to account for viscoelastic effects in the vocal-fold behavior, such as its strain-rate sensitivity and the stress hysteretic response typically measured during cyclic loading. This work is planned. The mechanical contribution of "active" myofibrils should also be modeled, so as to better understand the relative contribution of the *vocalis* and the *lamina propria* in the f_0 regulation. Finally, damage mechanisms could be studied by modifying the constitutive laws at the fiber scale.

CRediT authorship contribution statement

Alberto Terzolo: writing the original draft and designing the figures; theoretical developments and analyses, numerical implementation of the complete model and calculations. **Lucie Bailly:** direction of the overall project and design of the study; model conceptualization and verification of the results to help shaping the research and analyse the results; contributions to the writing of the original draft, and reviewing the manuscript; co-supervision of A.T. and T.C.; principal investigator for funding acquisition. **Laurent Orgéas:** design of the study; model conceptualization and verification of the results to help shaping the research and analyse the results; FE simulations of the stretching of corrugated beams; contributions to the writing of the original draft, and reviewing the manuscript; co-supervision of A.T. and T.C.; help for funding acquisition. **Thibaud Cochereau:** writing the original draft and designing the figures; main investigator of the experimental database chosen as a reference in the study; implementation of a prior version of the model and prior calculations. **Nathalie Henrich Bernardoni:** reviewing the manuscript; co-supervision of T.C.; help for funding acquisition.

Declaration of competing interest

The authors declare that they have no known competing financial interests or personal relationships that could have appeared to influence the work reported in this paper.

Acknowledgments

This work was supported by the LabEx Tec21 (Investissements d'Avenir – grant agreement n°ANR-11-LABX-0030), IDEX Univ. Grenoble Alpes, the ANR MicroVoice (grant n°ANR-17-CE19-0015-01), UGA-CNRS (grant AGIR-PEPS 2015 FIBROSCILLE), and Campus France (grant PHC Barrande n°38179WG).

Appendix A. Supplementary data

Supplementary material related to this article can be found online at https://doi.org/10.1016/j.jmbbm.2022.105118.

References

Arruda, E.M., Boyce, M.C., 1993. A three-dimensional constitutive model for the large stretch behavior of rubber elastic materials. J. Mech. Phys. Solids 41 (2), 389–412.
Asgari, M., Latifi, N., Heris, H.K., Vali, H., Mongeau, L., 2017. In vitro fibrillogenesis of tropocollagen type III in collagen type i affects its relative fibrillar topology and mechanics. Sci. Rep. 7 (1).
Bailly, L., Cochereau, T., Orgéas, L., Henrich Bernardoni, N., Rolland du Roscoat, S., McLeer-Florin, A., Robert, Y., Laval, X., Laurencin, T., Chaffanjon, P., Fayard, B., Boller, E., 2018. 3D multiscale imaging of human vocal folds using synchrotron X-ray microtomography in phase retrieval mode. Sci. Rep. 8 (1).
Bailly, L., Geindreau, C., Orgéas, L., Deplano, V., 2012. Towards a biomimetism of abdominal healthy and aneurysmal arterial tissues. J. Mech. Behav. Biomed. Mater. 10, 151–165.
Bailly, L., Toungara, M., Orgéas, L., Bertrand, E., Deplano, V., Geindreau, C., 2014. In-plane mechanics of soft architectured fibre-reinforced silicone rubber membranes. J. Mech. Behav. Biomed. Mater. 40, 339–353.
Basciano, C.A., Kleinstreuer, C., 2009. Invariant-based anisotropic constitutive models of the healthy and aneurysmal abdominal aortic wall. J. Biomech. Eng. 131 (2).
Beatty, M.F., 2003. An average-stretch full-network model for rubber elasticity. J. Elasticity 70 (1–3), 65–86.
Berry, D., Titze, I., 1996. Normal modes in a continuum model of vocal fold tissues. J. Acoust. Soc. Am. 100, 3345–3354.
Bickley, C., 1989. Acoustic Evidence for the Development of Speech (Ph.D. thesis). Massachusetts Institute of Technology, Cambridge.
Borg, T.K., Caulfield, J.B., 1980. Morphology of connective tissue in skeletal muscle. Tissue Cell 12, 197–207.
Boyce, M.C., Arruda, E.M., 2000. Constitutive models of rubber elasticity: A review. Rubber Chem. Technol. 73 (3), 504–523.
Brown, W.S., Morris, R.J., Hollien, H., Howell, E., 1991. Speaking fundamental frequency characteristics as a function of age and professional singing. J. Voice 5 (4), 310–315.

Buehler, M.J., 2008. Nanomechanics of collagen fibrils under varying cross-link densities: Atomistic and continuum studies. J. Mech. Behav. Biomed. Mater. 1 (1), 59–67.
Bühler, R.B., Sennes, L.U., Tsuji, D.H., Mauad, T., Ferraz Da Silva, L., Saldiva, P.N., 2011. Collagen type I, collagen type III, and versican in vocal fold lamina propria. Arch. Otolaryngol. - Head Neck Surg. 137 (6), 604–608.
Caillerie, D., Mourad, A., Raoult, A., 2006. Discrete homogenization in graphene sheet modeling. J. Elasticity 84 (1), 33–68.
Chan, R.W., 2018. Nonlinear viscoelastic characterization of human vocal fold tissues under large-amplitude oscillatory shear (LAOS). J. Rheol. 62 (3), 695–712.
Chan, R.W., Gray, S.D., Titze, I.R., 2001. The importance of hyaluronic acid in vocal fold biomechanics. Otolaryngol. Head Neck Surg. 124 (6), 607–614.
Chen, P.T., Thompson, L.D.V., Snow, L.A., 2006. Muscle structure and function. Orthop. Phys. Ther. Secrets 1–9.
Chen, H., Zhao, X., Lu, X., Kassab, G., 2013. Non-linear micromechanics of soft tissues. Int. J. Non-Linear Mech. 56, 79–85.
Cochereau, T., Bailly, L., Orgéas, L., Henrich Bernardoni, N., Robert, Y., Terrien, M., 2020. Mechanics of human vocal folds layers during finite strains in tension, compression and shear. J. Biomech. 110.
Colomo, F., Piroddi, N., Poggesi, C., Te Kronnie, G., Tesi, C., 1997. Active and passive forces of isolated myofibrils from cardiac and fast skeletal muscle of the frog. J. Physiol. 500 (2), 535–548.
Comninou, M., Yannas, I.V., 1976. Dependence of stress–strain nonlinearity of connective tissues on the geometry of collagen fibres. J. Biomech. 9 (7), 427–433.
Coughlan, C., Chou, L., Jing, J., Chen, J., Rangarajan, S., Chang, T.H., Sharma, G.K., Cho, K., Lee, D., Goddard, J.A., Chen, Z., Wong, B.J.F., 2016. In vivo cross-sectional imaging of the phonating larynx using long-range Doppler optical coherence tomography. Sci. Rep. 6 (22792), 1–9.
Csapo, R., Gumpenberger, M., Wessner, B., 2020. Skeletal muscle extracellular matrix – what do we know about its composition, regulation, and physiological roles? a narrative review. Front. Physiol. 11, 253, URL: https://www.frontiersin.org/article/10.3389/fphys.2020.00253.
Descout, R., Auloge, J.Y., Guerin, B., 1980. Continuous model of the vocal source. In: Proceedings of the 5th International Conference on Acoustics, Speech and Signal Processing. pp. 61–64.
Ekman, A., Miettinen, A., Tallinen, T., Timonen, J., 2014. Contact formation in random networks of elongated objects. Phys. Rev. Lett. 113, 268001, URL: https://link.aps.org/doi/10.1103/PhysRevLett.113.268001.
Finck, C., 2008. Implantation d'Acide Hyaluronique Estérifié Lors de la Microchirurgie des Lésions Cordales Bénignes (Ph.D. thesis). Université de Liège, Liège.
Finck, C.L., Harmegnies, B., Remacle, A., Lefebvre, P., 2010. Implantation of esterified hyaluronic acid in microdissected reinke's space after vocal fold microsurgery: Short- and long-term results. J. Voice 24 (5), 626–635.
Finck, C., Lefebvre, P., 2005. Implantation of esterified hyaluronic acid in microdissected reinke's space after vocal fold microsurgery: First clinical experiences. Laryngoscope 115 (10), 1841–1847.
Fratzl, P., 2008. Collagen: Structure and mechanics, an introduction. In: Collagen: Structure and Mechanics. Springer US, pp. 1–13.
Freed, A.D., Doehring, T.C., 2005. Elastic model for crimped collagen fibrils. J. Biomech. Eng. 127 (4), 587–593.
Garcia, J.A., Benboujja, F., Beaudette, K., Guo, R., Boudoux, C., Hartnick, C.J., 2016. Using attenuation coefficients from optical coherence tomography as markers of vocal fold maturation. Laryngoscope 126, E218–23.
Gasser, T.C., Ogden, R.W., Holzapfel, G.A., 2006. Hyperelastic modelling of arterial layers with distributed collagen fibre orientations. J. R. Soc. Interface 3 (6), 15–35.
Gautieri, A., Vesentini, S., Redaelli, A., Buehler, M.J., 2012. Viscoelastic properties of model segments of collagen molecules. Matrix Biol. 31 (2), 141–149.
Gelse, K., Pöschl, E., Aigner, T., 2003. Collagens - Structure, function, and biosynthesis. Adv. Drug Deliv. Rev. 55 (12), 1531–1546.
Gray, S.D., Titze, I.R., Chan, R., Hammond, T.H., 1999. Vocal fold proteoglycans and their influence on biomechanics. Laryngoscope 109 (6), 845–854.
Gunter, H.E., 2003. A mechanical model of vocal-fold collision with high spatial and temporal resolution. J. Acoust. Soc. Am. 113 (2), 994–1000.
Hahn, M.S., Kobler, J.B., Starcher, B.C., Zeitels, S.M., Langer, R., 2006a. Quantitative and comparative studies of the vocal fold extracellular matrix I: Elastic fibers and hyaluronic acid. Ann. Otol. Rhinol. Laryngol. 115 (2), 156–164.
Hahn, M.S., Kobler, J.B., Zeitels, S.M., Langer, R., 2006b. Quantitative and comparative studies of the vocal fold extracellular matrix II: Collagen. Ann. Otol. Rhinol. Laryngol. 115 (3), 225–232.
Hammond, T.H., Zhou, R., Hammond, E.H., Pawlak, A., Gray, S.D., 1997. The intermediate layer: A morphologic study of the elastin and hyaluronic acid constituents of normal human vocal folds. J. Voice 11 (1), 59–66.
Hantzakos, A., Remacle, M., Dikkers, F.G., Degols, J.C., Delos, M., Friedrich, G., Giovanni, A., Rasmussen, N., 2009. Exudative lesions of Reinke's space: A terminology proposal. Eur. Arch. Oto-Rhino-Laryngol. 266 (6), 869–878.
Heris, H.K., Rahmat, M., Mongeau, L., 2012. Characterization of a hierarchical network of hyaluronic acid/gelatin composite for use as a smart injectable biomaterial. Macromol. Biosci. 12 (2), 202–210.
Herrera, V.L., Viereck, J.C., Lopez-Guerra, G., Kumai, Y., Kobler, J., Karajanagi, S., Park, H., Hillman, R., Zeitels, S.M., 2009. Tesla magnetic resonance microimaging of laryngeal tissue architecture. Laryngoscope 119 (11), 2187–2194.
Hirano, M., 1974. Morphological structure of the vocal cord as a vibrator and its variations. Folia Phoniatr. Logop. 26 (2), 89–94.
Hollingsworth, N.T., Wagner, D.R., 2011. Modeling shear behavior of the annulus fibrosus. J. Mech. Behav. Biomed. Mater. 4 (7), 1103–1114.
Holzapfel, G.A., Gasser, T.C., Ogden, R.W., 2000. A new constitutive framework for arterial wall mechanics and a comparative study of material models. J. Elasticity 61 (1–3), 1–48.
Kastelic, J., Palley, I., Baer, E., 1980. A structural mechanical model for tendon crimping. J. Biomech. 13 (10), 887–893.
Kazarine, A., Kolosova, K., Gopal, A.A., Wang, H., Tahara, R., Rammal, A., Kost, K., Mongeau, L., Li-Jessen, N.Y.K., Wiseman, P.W., 2019. Multimodal virtual histology of rabbit vocal folds by nonlinear microscopy and nano computed tomography. Biomed. Opt. Express 10, 1151–1164.
Kelleher, J.E., Siegmund, T., Du, M., Naseri, E., Chan, R.W., 2013a. Empirical measurements of biomechanical anisotropy of the human vocal fold lamina propria. Biomech. Model. Mechanobiol. 12 (3), 555–567.
Kelleher, J.E., Siegmund, T., Du, M., Naseri, E., Chan, R.W., 2013b. The anisotropic hyperelastic biomechanical response of the vocal ligament and implications for frequency regulation: A case study. J. Acoust. Soc. Am. 133 (3), 1625–1636.
Klepacek, I., Jirak, D., Duskova Smrckova, M., Janouskova, O., Vampola, T., 2016. The human vocal fold layers. Their delineation inside vocal fold as a background to create 3D digital and synthetic glottal model. J. Voice 30 (5), 529–537.
Kobler, J.B., Chang, E.W., Zeitels, S.M., Yun, S-H., 2010. Dynamic imaging of vocal fold oscillation with four-dimensional optical coherence tomography. Laryngoscope 120, 1354–1362.
Krook, M.I.P., 1988. Speaking fundamental frequency characteristics of normal Swedish subjects obtained by glottal frequency analysis. Folia Phoniatr. Logop. 40 (2), 82–90.
Lanir, Y., 1978. Structure-strength relations in mammalian tendon. Biophys. J. 24 (2), 541–554.
Lanir, Y., 1979. A structural theory for the homogeneous biaxial stress–strain relationships in flat collagenous tissues. J. Biomech. 12 (6), 423–436.
Lanir, Y., 1983. Constitutive equations for fibrous connective tissues. J. Biomech. 16 (1), 1–12.
Lieber, R.L., 1986. Skeletal muscle adaptability. I: Review of basic properties. Dev. Med. Child Neurol. 28 (3), 390–397.
Limbert, G., Middleton, J., 2006. A constitutive model of the posterior cruciate ligament. Med. Eng. Phys. 28 (2), 99–113.
Lin, D.H., Yin, F.C., 1998. A multiaxial constitutive law for mammalian left ventricular myocardium in steady-state barium contracture or tetanus. J. Biomech. Eng. 120 (4), 504–517.
Lorenzo, A.C., Caffarena, E.R., 2005. Elastic properties, Young's modulus determination and structural stability of the tropocollagen molecule: A computational study by steered molecular dynamics. J. Biomech. 38 (7), 1527–1533.
Maceri, F., Marino, M., Vairo, G., 2010a. A unified multiscale mechanical model for soft collagenous tissues with regular fiber arrangement. J. Biomech. 43 (2), 355–363.
Maceri, F., Marino, M., Vairo, G., 2010b. From cross-linked collagen molecules to arterial tissue: a nano-micro-macroscale elastic model. Acta Mech. Solida Sin. 23 (S1), 98–108.
Maceri, F., Marino, M., Vairo, G., 2013. Age-dependent arterial mechanics via a multiscale elastic approach. Int. J. Comput. Methods Eng. Sci. Mech. 14 (2), 141–151.
Magid, A., Law, D.J., 1985. Myofibrils bear most of the resting tension in frog skeletal muscle. Science 230 (4731), 1280–1282.
Marino, M., Vairo, G., 2012. Equivalent stiffness and compliance of curvilinear elastic fibers. In: Lecture Notes in Applied and Computational Mechanics, Vol. 61. pp. 309–332.
Marino, M., Vairo, G., 2013. Multiscale elastic models of collagen bio-structures: from cross-linked molecules to soft tissues. Stud. Mechanobiol. Tissue Eng. Biomater. 14, 73–102.
Marino, M., Vairo, G., 2014a. Computational modeling of soft tissues and ligaments. Comput. Model. Biomech. Biotribol. Musculoskelet. Syst.: Biomater. Tissues 81 (5), 141–172.
Marino, M., Vairo, G., 2014b. Stress and strain localization in stretched collagenous tissues via a multiscale modelling approach. Comput. Methods Biomech. Biomed. Eng. 17 (1), 11–30.
Marino, M., Wriggers, P., 2017. Finite strain response of crimped fibers under uniaxial traction: An analytical approach applied to collagen. J. Mech. Phys. Solids 98, 429–453.
Maturo, S., Benboujja, F., Boudoux, C., Hartnick, C., 2012. Quantitative distinction of unique vocal fold subepithelial architectures using optical coherence tomography. Ann. Otol. Rhinol. Laryngol. 121, 754–760.
May-Newman, K., Lam, C., Yin, F.C., 2009. A hyperelastic constitutive law for aortic valve tissue. J. Biomech. Eng. 131 (8).
Madruga de Melo, E.C., Lemos, M., Aragão Ximenes Filho, J., Sennes, L.U., Nascimento Saldiva, P.H., Tsuji, D.H., 2003. Distribution of collagen in the lamina propria of the human vocal fold. Laryngoscope 113 (December), 2187–2191.
Miri, A.K., Barthelat, F., Mongeau, L., 2012. Effects of dehydration on the viscoelastic properties of vocal folds in large deformations. J. Voice 26 (6), 688–697.

Miri, A.K., Heris, H.K., Mongeau, L., Javid, F., 2014. Nanoscale viscoelasticity of extracellular matrix proteins in soft tissues: A multiscale approach. J. Mech. Behav. Biomed. Mater. 30, 196–204.

Miri, A.K., Heris, H.K., Tripathy, U., Wiseman, P.W., Mongeau, L., 2013. Microstructural characterization of vocal folds toward a strain–energy model of collagen remodeling. Acta Biomater. 9 (8), 7957–7967.

Mukund, K., Subramaniam, S., 2020. Skeletal muscle: A review of molecular structure and function, in health and disease. Wiley Interdiscip. Rev.: Syst. Biol. Med. 12 (1).

Natali, A.N., Carniel, E.L., Gregersen, H., 2009. Biomechanical behaviour of oesophageal tissues: Material and structural configuration, experimental data and constitutive analysis. Med. Eng. Phys. 31 (9), 1056–1062.

Nierenberger, M., Rémond, Y., Ahzi, S., 2013. A new multiscale model for the mechanical behavior of vein walls. J. Mech. Behav. Biomed. Mater. 23, 32–43.

Ogden, R.W., Saccomandi, G., 2007. Introducing mesoscopic information into constitutive equations for arterial walls. Biomech. Model. Mechanobiol. 6 (5), 333–344.

Orgéas, L., Favier, D., Rio, G., 1998. Déformation superélastique non homogène d'une éprouvette de traction NiTi. Expérience et modélisation numérique. Rev. Eur. Elém. Finis 7 (8), 111–136.

Peng, X.Q., Guo, Z.Y., Moran, B., 2006. .An anisotropic hyperelastic constitutive model with fiber–matrix shear interaction for the human annulus fibrosus. J. Appl. Mech. Trans. ASME 73 (5), 815–824.

Pinsky, P.M., Van Der Heide, D., Chernyak, D., 2005. .Computational modeling of mechanical anisotropy in the cornea and sclera. J. Cataract. Refract. Surg. 31 (1), 136–145.

Potier-Ferry, M., Siad, L., 1992. Homogénéisation géométrique d'une poutre ondulée. (Geometrical homogenization of a corrugated beam). C. R. Acad. Sci., Paris II T314, 425–430.

Roberts, T., Morton, R., Al-Ali, S., 2011. Microstructure of the vocal fold in elderly humans. Clin. Anat. 24 (5), 544–551.

Rodney, D., Fivel, M., Dendievel, R., 2005. Discrete modeling of the mechanics of entangled materials. Phys. Rev. Lett. 95, 108004.

Rodney, D., Gadot, B., Martinez, O.R., Du Roscoat, S.R., Orgéas, L., 2016. Reversible dilatancy in entangled single-wire materials. Nature Mater. 15 (1), 72–77.

Rohlfs, A.K., Goodyer, E., Clauditz, T., Hess, M., Kob, M., Koops, S., Püschel, K., Roemer, F.W., Müller, F., 2013. The anisotropic nature of the human vocal fold: An ex vivo study. Eur. Arch. Oto-Rhino-Laryngol. 270 (6), 1885–1895.

Sato, K., Hirano, M., Nakashima, T., 2002. Age-related changes of collagenous fibers in the human vocal fold mucosa. Ann. Otol. Rhinol. Laryngol. 111 (1), 15–20.

Sato, T., Tauchi, H., 1982. Age changes in human vocal muscle. Mech. Ageing Dev. 18 (1), 67–74.

Shen, Z.L., Dodge, M.R., Kahn, H., Ballarini, R., Eppell, S.J., 2008. Stress–strain experiments on individual collagen fibrils. Biophys. J. 95 (8), 3956–3963.

Subramanian, G., Picu, C.R., 2011. Mechanics of three-dimensional, nonbonded random fiber networks. Phys. Rev. Lett. 83, 108004, URL: https://link.aps.org/doi/10.1103/PhysRevE.83.056120.

Tao, C., Jiang, J.J., 2007. Mechanical stress during phonation in a self-oscillating finite-element vocal fold model. J. Biomech. 40 (10), 2191–2198.

Tateya, T., Tateya, I., Bless, D.M., 2006. Collagen subtypes in human vocal folds. Ann. Otol. Rhinol. Laryngol. 115 (6), 469–476.

Titze, I.R., Hunter, E.J., 2004. Normal vibration frequencies of the vocal ligament. J. Acoust. Soc. Am. 115 (5), 2264–2269.

Treloar, L., 1943. The elasticity of a network of long chain molecules (i and ii). Trans. Faraday Soc. 39, 36–64, 241–246.

Vampola, T., Horáček, J., Klepáček, I., 2016. Computer simulation of mucosal waves on vibrating human vocal folds. Biocybern. Biomed. Eng. 36 (3), 451–465.

Ward, S.R., Winters, T.M., O'Connor, S.M., Lieber, R.L., 2020. Non-linear scaling of passive mechanical properties in fibers, bundles, fascicles and whole rabbit muscles. Front. Physiol. 11.

Weiß, S., Thomson, S.L., Lerch, R., Döllinger, M., Sutor, A., 2013. Pipette aspiration applied to the characterization of nonhomogeneous, transversely isotropic materials used for vocal fold modeling. J. Mech. Behav. Biomed. Mater. 17, 137–151.

Yang, L., 2008. Mechanical Properties of Collagen Fibrils and Elastic Fibers Explored by AFM (Ph.D. thesis). University of Twente, Enschede.

Yang, L., Van Der Werf, K.O., Fitié, C.F., Bennink, M.L., Dijkstra, P.J., Feijen, J., 2008. Mechanical properties of native and cross-linked type I collagen fibrils. Biophys. J. 94 (6), 2204–2211.

Zhang, K., Siegmund, T., Chan, R.W., 2007. A two-layer composite model of the vocal fold lamina propria for fundamental frequency regulation. J. Acoust. Soc. Am. 122 (2), 1090–1101.

Zhang, K., Siegmund, T., Chan, R.W., Fu, M., 2009. Predictions of fundamental frequency changes during phonation based on a biomechanical model of the vocal fold lamina propria. J. Voice 23 (3), 277–282.